Sulfur-doping/leaching induced structural transformation toward boosting electrocatalytic water splitting

Xiang Chen [a,b,*], Zhaojian Qiu [a,b], Hanlu Xing [b], Shunxin Fei [b], Junzhe Li [b], Lianbo Ma [a,b], Yongtao Li [a,b], Dongming Liu [a,b,*]

[a] Key Laboratory of Green Fabrication and Surface Technology of Advanced Metal Materials (Anhui University of Technology), Ministry of Education, Maanshan 243002, PR China
[b] School of Materials Science and Engineering, Anhui University of Technology, Maanshan 243002, PR China

ARTICLE INFO

ABSTRACT

Rational modulation for the composition and structure of the oxygen evolution reaction (OER) electrocatalysts is crucial for overall water splitting. Herein, how to utilize composition change and structure reconstruction via an in situ nonmetal element-doping and leaching-induced strategy to develop robust water oxidation catalysts is firstly proposed. The as-obtained Ni-FeOOH with structural transformation presents a remarkable OER activity with an overpotential of 224 mV at 100 mA/cm^2, which is much superior to undoped or unleached catalysts. By tuning the amount of S, the S-doped NiFe-based catalyst exhibits an overpotential of 168 mV at 100 mA/cm^2 for the hydrogen evolution reaction. The electrocatalysts with tunable bifunctionality requires only 1.43 V to drive 10 mA/cm^2 towards overall water splitting. Systematic experiments and characterizations demonstrate that structural reconstruction into highly active oxyhydroxides species and sufficient activation of lattice oxygen redox reactivity are responsible for the fascinating OER activity induced by S doping/leaching.

1. Introduction

Electrochemical water splitting has been demonstrated to be a potential route to convert intermittent renewable such as sunlight, tidal, wind, and hydropower energies into storable hydrogen energy [1–3]. The oxygen evolution reaction (OER) with four-electron-transfer process limits the energy conversion efficiency of overall water electrolysis due to its sluggish kinetics [4–6]. Hence, a lot of efforts have been endeavored to develop more high-performance catalysts for the OER processes. Up to now, some precious metal oxides such as IrO$_2$ and RuO$_2$ are considered as the efficient OER electrocatalysts owing to their superior performances [6,7]. However, the high cost and low reserves of these precious metal-based catalysts limit their practical applications. Thus, the design and development of low-cost and high-efficiency OER electrocatalysts is highly desirable.

Among the reported OER catalysts, 3d transition-metal-based materials (such as Ni, Fe, Co, *etc*) have attracted more and more attention on account of their earth-abundant reserves and low OER overpotentials [8–15]. To further enhance their OER activities, it is pivotal to cognize the influence of chemical composition and structure on the electro-catalytic performance and their changes during the OER process. Recently, most nonnoble metal-based OER catalysts (such as transition-metal pnictides and chalcogenides) are reported to occur structure reconstruction into metal oxyhydroxide as the active species [16]. For example, Zhang et. al found that the leaching of fluoride could promote in situ surface self-reconstruction and convert the pristine NiFe-OH-F into amorphous and porous metal oxide under OER process [17]. However, the structure-performance relationship has not been completely understood in terms of surface reconstruction during the OER conditions [18,19]. For the transition metal-based catalysts, the electronic structure of cations has an important role in the OER performance and thus the cations are generally considered as the active sites and interact with the oxygen-containing species [20,21]. On the other hand, the anions also are regarded to modify the electronic structure of adjacent metal active sites [22,23]. In consequence, it is of great significance to rationally tune the chemical environment and structure of anions and cations of transition metal-based catalysts for obtaining a remarkable electrocatalytic OER activity.

---

* Corresponding authors at: Key Laboratory of Green Fabrication and Surface Technology of Advanced Metal Materials (Anhui University of Technology), Ministry of Education, Maanshan 243002, PR China.
  E-mail addresses: chxiang@mail.ustc.edu.cn (X. Chen), ldm_ahut@163.com (D. Liu).

Herein, the S-doped NiFe layered double hydroxides (LDHs) nanosheets (denoted as NFO-S*x*, *x* represents the amount of sulfur-containing precursor added during the preparation of the sample) on iron foam (IF) were fabricated by a one-pot hydrothermal method (Scheme 1), and a phenomenon that the S in NiFe LDHs can leach out during the OER process and then induce chemical evolution and in situ structure self-reconstruction was reported for the first time. After the electrochemical modification under OER conditions, as shown in Scheme 1, almost all S was removed from S-doped NiFe LDHs and the original nanosheets in small size were transformed into Ni-doped FeOOH nanosheets (denoted as O-NFO-S*x*) with larger size, which possesses highly active OER species oxyhydroxides [18,24]. However, there is no structural rearrangement for the catalyst without S doping during OER process, and thus it can be confirmed that the leaching of S facilitates the structure transformation under electrochemical OER conditions. The electrocatalytic OER performance of the S-doped NiFe-based catalyst with structure reconstruction was improved remarkably compared with the original undoped or unleached samples. Besides, by tailoring the amount of the S-containing precursor, S-incorporated NiFe-based catalyst shows an excellent hydrogen evolution reaction (HER) activity under optimal conditions. Furthermore, a two-electrode electrochemical cell for full water splitting assembling with the best-performing OER and HER electrocatalysts only requires a low cell voltage of 1.43 V to achieve a current density$_{\text{geo}}$ (current normalized by geometric area) of 10 mA/cm^2, which is superior to most ever reported cell voltages for overall water splitting based on the earth-abundant 3*d* transition-metal-based electrocatalysts. Based on a series of component, structural and mechanism characterizations and analysis, the electrocatalytic mechanism responsible for the fascinating water splitting activity was investigated and proposed.

2. Experimental section

2.1. Synthesis of NFO-Sx electrocatalysts

In a typical process, a mixture of 180 mg Ni(NO$_3$)$_2$, *x* (*x* = 3, 5, 10, 40, 60 and 80) mg Na$_2$S$_2$O$_3$, and 0.5 × 1.5 cm iron foam (IF) were added into a 100 mL Teflon-lined stainless-steel autoclave with 40 mL of deionized water and heated at 120 °C for 5 h. After being cooled to room temperature, the as-prepared products were washed with deionized water to remove the residual solution on the surface. Then the product was obtained after heating at 40 °C for 12 h in vacuum, which was marked as NFO-S*x* for simplicity. For comparisons, the catalyst without

adding Na$_2$S$_2$O$_3$ was synthesized (denoted as NFO) and the electrode prepared by just heating IF (denoted as FO) while the other conditions remained unchanged.

2.2. Materials characterization

X-ray diffraction (XRD) tests of the as-obtained samples were performed by using a Bruker D8 Advance X-ray diffractometer (Cu Kα radiation, λ = 1.5406 nm) at a scan rate of 5°/min. The morphological characterizations of the samples were carried out by utilizing a field-emission scanning electron microscope (SEM) (JEOL JSM6335) operating under 20 kV. Transmission electron microscopy (TEM) and elemental mapping images of the samples were obtained by using a JEOL JEM 2100 system (200 kV). X-ray photoelectron spectroscopy (XPS) measurements were carried out via an ESCALAB 250 X-ray photoelectron spectrometer (Thermo-VG Scientific) with Al Kα X-ray radiation. Raman spectroscopy tests were carried out by using a Renishaw inVia.

2.3. Electrochemical measurements

Electrochemical performances were measured via a typical three-electrode system by employing a CHI-660E electrochemical workstation (CH Instruments, Shanghai, China). The NFO-S*x* on IF were applied as the work electrodes (the geometric area is 0.25 cm^2). Hg/HgO and graphite rod were used as the reference and counter electrodes, respectively. A freshly prepared 1 M KOH aqueous solution (pH=14) was employed as the electrolyte. All collected potentials were normalized based on the reversible hydrogen electrode (RHE) via the following equation: $E_{\text{RHE}} = E_{\text{Hg/HgO}} + 0.059 \times \text{pH} + 0.098$. Linear sweep voltammetry (LSV) plots were obtained in a 1 M KOH electrolyte at a scan rate of 5 mV/s with 90% *iR* correction. Ten cyclic voltammetry (CV) cycles were used to activate the electrodes at a scan rate of 5 mV/s before LSV collection. The electrochemical impedance spectroscopy (EIS) measurements were operated on the same three-electrode device with an AC impedance over the frequency range from 0.01 to 10^5 Hz at the potential of 0.52 and −1.1 V vs. Hg/HgO for the OER and HER systems, respectively. The electrochemical surface areas (ECSAs) were calculated according to the following equation: ECSA = $C_{\text{dl}}/C_{\text{s}} \times A$, where C_{dl} is the double-layer capacitance, which can be estimated from the CV curves at different scan rates from 10 to 50 mV/s in the potential range of 0–0.1 V vs. Hg/HgO, the value of C_{s} is supposed to be 0.04 mF/cm^2 in 1 M KOH, and *A* represents the actual area of the efficient
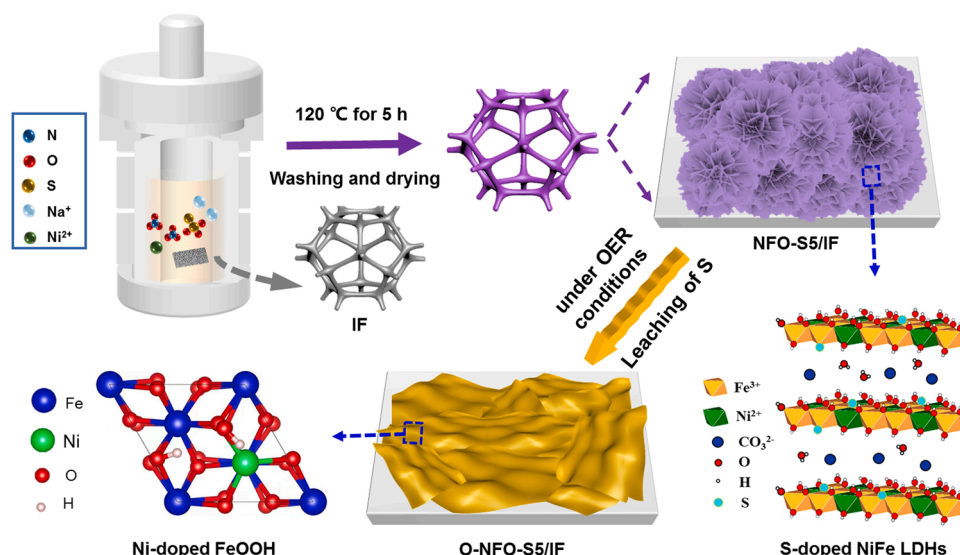
Scheme 1. Schematic representation of the preparation processes and the structures of NFO-S5 and O-NFO-S5 samples.

working electrode. For the overall water splitting cell, a two-electrode system was constructed by using NFO-Sx as the anode or cathode and then the LSV tests were carried out in a 1 M KOH electrolyte at a scan rate of 5 mV/s without *iR* compensation. The Faradic efficiency was obtained by the calculation according to the following equation: Faradic efficiency = [zF× (nH$_2$ or nO$_2$)]/Q, whereas z is the number of electron involved in the reaction (2 for H$_2$ and 4 for O$_2$), (nH$_2$ or nO$_2$) represents the number of mole H$_2$ or O$_2$ calculated approximately by the Ideal Gas Law, Q is the charge consumed during the electrolysis process (Q = I × t, I is a given value of a constant applied current in the test and t is the oxidation time (s) under the constant applied current), and F is the Faraday constant (96,485 C/mol).

3. Results and discussion

3.1. Morphology and structure of NFO-Sx

The S-doped nickel-iron hydroxides (NFO-S) were firstly prepared on 3D iron foam (IF) via a facile one-pot hydrothermal method by using 180 mg Ni(NO$_3$)$_2$, x (x = 3, 5, 10, 40, 60 and 80) mg Na$_2$S$_2$O$_3$, and 0.5 × 1.5 cm IF as the Ni, S and Fe precursors, respectively, and the as-obtained samples as are denoted as NFO-Sx for simplicity. For comparison, the catalyst without adding Na$_2$S$_2$O$_3$ was synthesized, which is denoted as NFO, and the electrode prepared by just heating IF is denoted as FO. The X-ray diffraction (XRD) pattens (Fig. S1) and scanning electron microscope (SEM) images (Fig. S2) of FO and pristine IF show that a layer of Fe$_2$O$_3$ particles is formed on the surface of IF. When Ni(NO$_3$)$_2$ was added into the Teflon reactor, the as-prepared NFO was composed

of NiFe LDHs nanosheets and Fe$_2$O$_3$ particles from the SEM and Transmission electron microscopy (TEM) images (Fig. S3) and XRD patten (Fig. 1a) of NFO. Further, it can be found from their XRD patterns (Figs. S4 and 1a) and SEM images (Figs. S5 and 1b, c) that the composition of the as-synthesized samples would change with the content of Na$_2$S$_2$O$_3$. When low amount of Na$_2$S$_2$O$_3$ was used, the content of Fe$_2$O$_3$ particles decreased and the content of LDHs nanosheets increased with the increase of Na$_2$S$_2$O$_3$. And if a large number of Na$_2$S$_2$O$_3$ was added, a new phase of Ni$_3$S$_2$ would form, the Fe$_2$O$_3$ particles disappeared, and the content of LDHs decreased. As shown in Fig. 1, it can be observed that the NFO-S5 sample is consisted of a lot of NiFe LDHs nanosheets and a little Fe$_2$O$_3$ from the XRD, SEM, TEM, HRTEM, SAED and element mapping images. Compared with NFO, the chemical structure of NFO-Sx has been changed because of the doping of S, and thus it is essential and significant to investigate the influences of the doping of S on the OER performance and the leaching of S on the structure reconstruction during OER process.

3.2. Electrochemical OER activities of NFO-Sx and O-NFO-Sx

The electrocatalytic OER performances of NFO-Sx catalysts were evaluated as shown in Fig. 2a. In this work, unless otherwise indicated, the electrocatalytic activity of the as-prepared samples are normalized based on the geometric area of the effective working electrode. The NFO-S5 exhibits the highest OER activity. Current density$_{geo}$ of 100 mA/cm^2 is obtained at the lowest overpotential of 232 mV, which is much superior to that of undoped NFO (267 mV) at the same current density$_{geo}$ as summarized in Fig. 2b. With the increase of the content of S, the
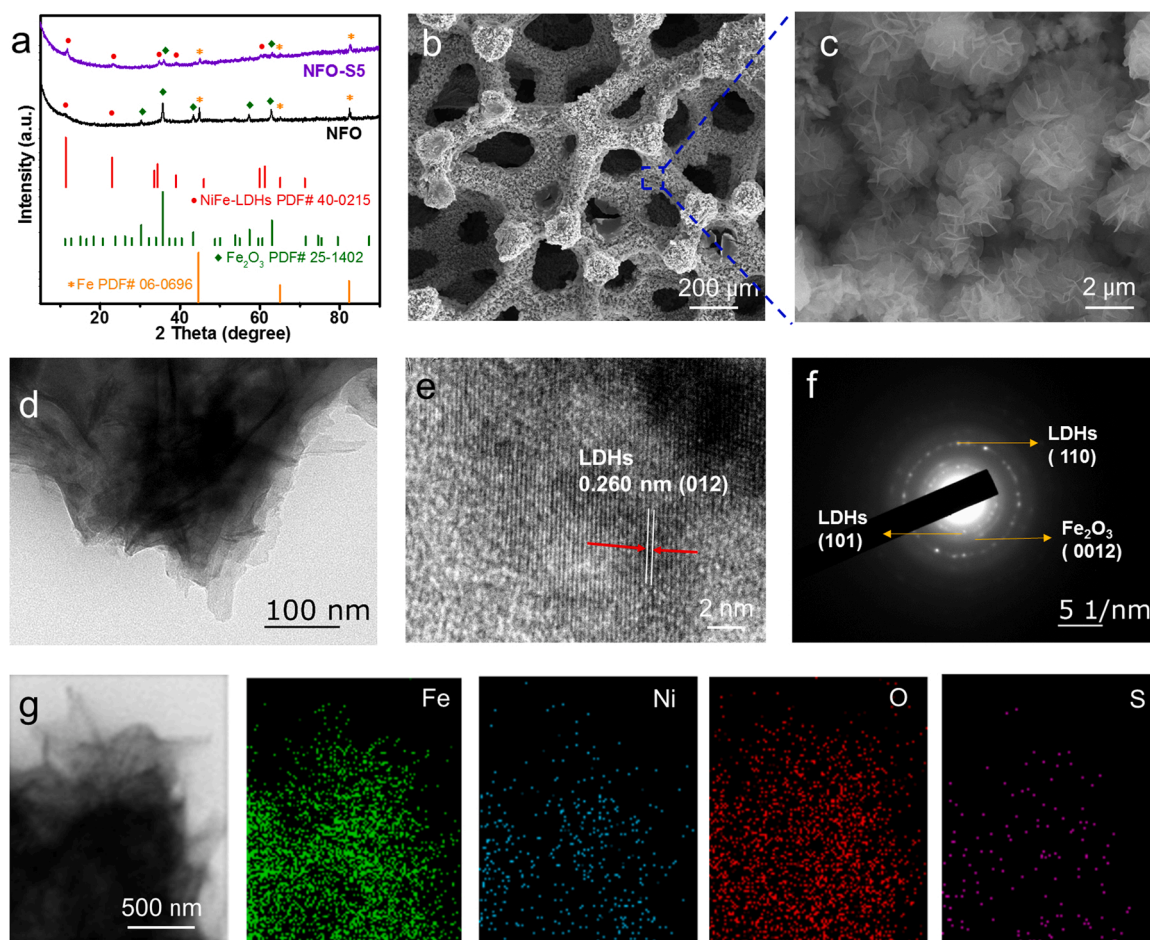

Fig. 1. (a) XRD pattens of NFO and NFO-S5, (b, c) SEM images, (d) TEM image, (e) HRTEM image, (f) selected area electron diffraction (SAED) image and (g) elemental mapping images of Fe, Ni, O and S of NFO-S5.
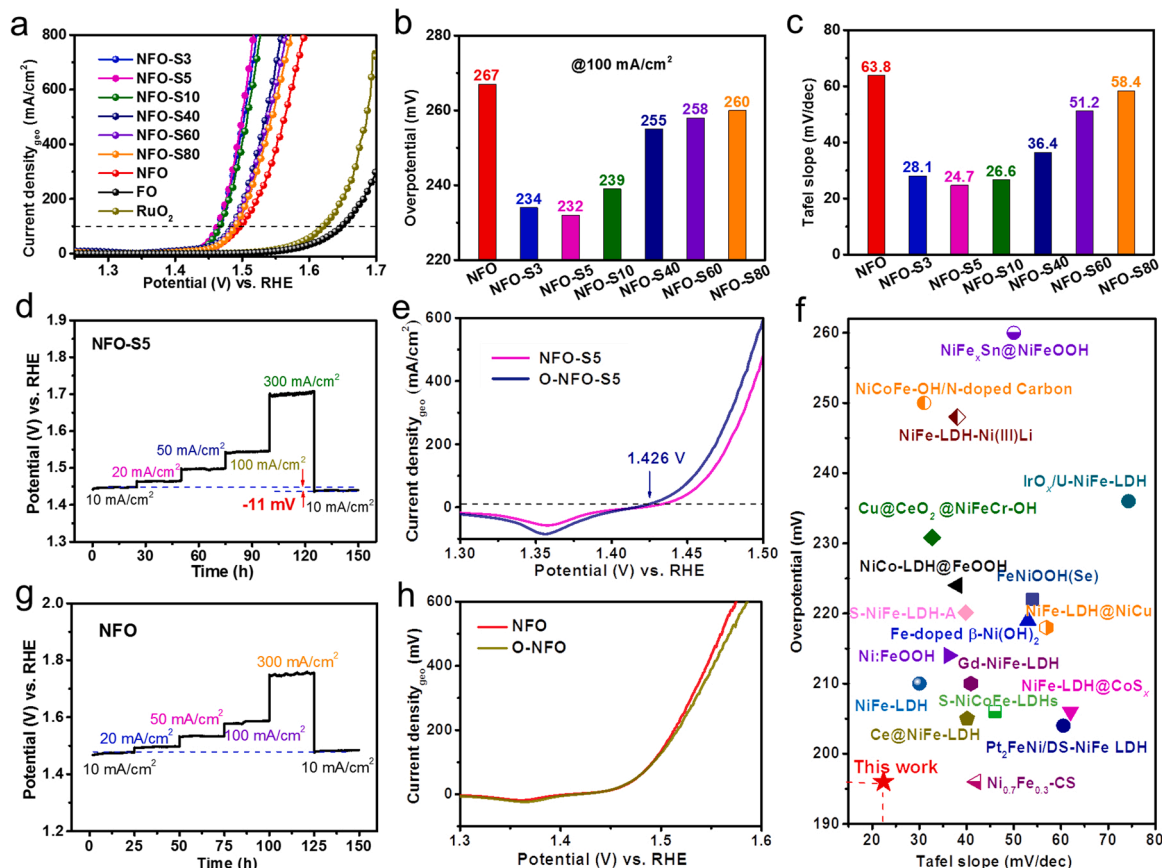
Fig. 2. (a) LSV curves for the OER, (b) overpotential comparison at the current density$_{geo}$ of 100 mA/cm^2 and (c) Summarized Tafel slopes of NFO-S*x* derived from steady state chronoamperometric measurements. (d) Chronopotentiometry of NFO-S5 at the current densities$_{geo}$ of 10, 20, 50, 100, 300 and 10 mA/cm^2 for a total time of 150 h. (e) LSV curves of NFO-S5 before and after OER stability test. (f) Comparison of the overpotentials at the current density$_{geo}$ of 10 mA/cm^2 and Tafel slopes of O-NFO-S5 with other recent reported NiFe-based OER electrocatalysts. (g) Chronopotentiometry of NFO at the current densities$_{geo}$ of 10, 20, 50, 100, 300 and 10 mA/cm^2 for a total time of 150 h. (h) LSV curves of NFO before and after OER stability test.

OER activity of NFO-S*x* tends to deteriorate mainly due to the decrease of LDHs species. Fig. 2c presents that the Tafel slope (Here, the Tafel curves of the samples for the OER are derived from steady state chronoamperometric measurements [25] as shown in Figs. S6–S12) achieved on the undoped NFO electrocatalyst is 63.8 mV/dec, while much lower values of 28.1, 24.7, 26.6, 36.4, 51.2 and 58.4 mV/dec are obtained on NFO-S3, NFO-S5, NFO-S10, NFO-S40, NFO-S60 and NFO-S80, respectively. This can be attributed to the improved microelectronic environment of the metal active sites in the NFO-S*x* catalysts because of the incorporation of S, which will modulate the adsorption energies of the OER intermediates and therefore promote the OER kinetics [22,23,26].

The long-term chronopotentiometric durability of the optimized OER catalyst NFO-S5 was tested for six continuous stages at current densities$_{geo}$ of 10, 20, 50, 100, 300, and 10 mA/cm^2 for a total time of 150 h (Fig. 2d). Interestingly, in the last stage, a current density$_{geo}$ 10 mA/cm^2 requires ~ 11 mV less than the first stage, which can also be confirmed by the OER linear sweep voltammetry (LSV) curves before and after OER stability measurement as presented in Fig. 2e. The enhanced activity after OER test can also be demonstrated by the chronoamperometric stability measurement as shown in Fig. S13, suggesting after four continuous stages at the potentials of 1.48, 1.52, 1.56, and 1.60 V vs. RHE, in the last stage, the obtained current density$_{geo}$ is ~ 7.5 mA/cm^2 higher than the first stage. The overpotential of NFO-S5 after OER stability test (denoted as O-NFO-S5) at the current density$_{geo}$ of 10 mA/cm^2 is 196 mV and its corresponding Tafel slope is 22.8 mV/dec (Fig. S14), both of which are lower than those of NFO-S5 before OER stability test (an overpotential of 207 mV at 10 mA/cm^2 and a Tafel slope of 24.7 mV/dec). Such low overpotential and small

Tafel slope are dramatically improved relative to undoped or unleached catalysts and comparable to other recent reported NiFe-based OER catalysts as shown in Fig. 2f and Table S1. Besides, the best-performing OER catalyst O-NFO-S5 possesses excellent long-term durability over 100 h as presented in the chronoamperometric stability measurement (Fig. S15). However, for the NFO catalyst without S doping, the long-term OER durability measurement (Fig. 2g) and the LSV curves before and after OER stability test (Fig. 2h) indicate the OER activity of NFO could not be boosted by electrochemical OER durability test. Therefore, it is crucial to reveal the effect of S on the composition and structure change of NFO-S5 during the working conditions for understanding the mechanism responsible for the improvement of OER activity after electrochemical modification.

3.3. Effects of S-leaching on the morphology and structure of NFO-S*x*

To illuminate the impact of S on the structure of NFO-S5 under OER conditions, the XRD pattern of O-NFO-S5 was carried out and the result indicates that most of the LDHs crystal structure is converted to the Fe-oxyhydroxide (FeOOH) phase (Fig. 3a), and the transition-metal oxyhydroxides have been demonstrated to be highly active OER species [18, 24]. The SEM image with low magnification (Fig. 3b) of O-NFO-S5 is the same as NFO-S5, while the magnified SEM (Fig. 3c) and TEM images of O-NFO-S5 (Fig. 3d) display that its nanosheets are much larger than those of NFO-S5. As shown in Fig. 3e, the lattice spacings of 0.245 and 0.255 nm are attributed to the planes of (200) and (101) of FeOOH, respectively. Noteworthy, the XRD pattern (Fig. S16a) and SEM image (Fig. S16b) of the NFO catalyst after OER stability test demonstrate that
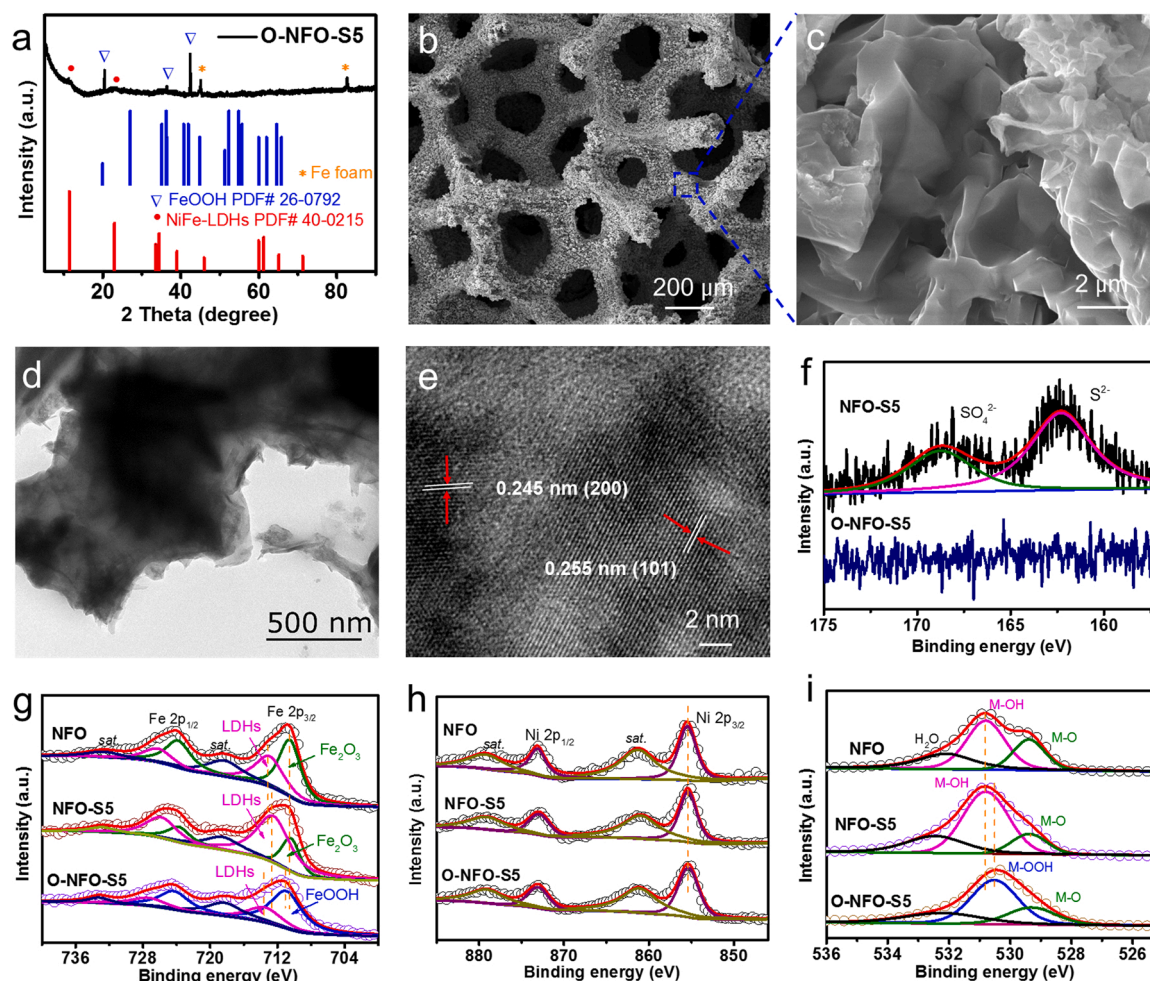
Fig. 3. (a) XRD patten, (b, c) SEM images, (d) TEM image and (e) HRTEM image of O-NFO-S5. (f) S 2p, (g) Fe 2p, (h) Ni 2p and (i) O 1s XPS spectra of NFO, NFO-S5 and O-NFO-S5.

both the crystal structure and morphology of NFO are almost unchanged under OER conditions. These results suggest that the crystal and morphological structures of NFO-S5 have been reconstructed owing to the leaching of S from the catalyst during the OER stability test.

The effects of S doping and leaching on the surface chemical components and oxidation states of the electrocatalysts were investigated by X-ray photoelectron spectroscopy (XPS) measurements. Fig. 3f shows that the two peaks centered at 168.8 and 162.4 eV of NFO-S5 catalyst are attributed to S^{2-} and SO_4^{2-}, respectively [27]. The S 2p XPS spectra of O-NFO-5 with no detectable signals confirms that almost all the S was leached from NFO-S5 catalyst after OER durability test. As indicated in Fig. 3g, in the Fe 2p XPS spectrum of NFO, the main peaks located at ca. 711 and 724 eV are assigned to Fe $2p_{3/2}$ and Fe $2p_{1/2}$, respectively, and those at ca. 718 and 733 eV are attributed to their satellite peaks. The Fe $2p_{3/2}$ peak could be deconvoluted into two peaks at 710.6 and 713.1 eV corresponding to Fe_2O_3 and LDHs, respectively [28–30]. After the doping of S, the location of Fe_2O_3 has no change while the peak of LDHs shows a 0.4 eV negative shift relative to NFO due to the doping of S. As for the O-NFO-S5 sample, the peak of Fe $2p_{3/2}$ could be deconvoluted to two peaks situated at 711.1 and 713.6 eV, which are ascribed to FeOOH and LDHs, respectively. The peak of LDHs exhibits a 0.9 eV positive shift and its intensity decreases obviously compared with those of NFO-S5 because of the leaching of S and structure transformation. For the Ni 2p XPS spectra (Fig. 3h), the peaks of NFO, NFO-S5, and O-NFO-S5 have no obvious difference with each other, suggesting S doping and leaching have no significant impact on the oxidation state of Ni. In addition, the oxidation states of metal Fe and Ni of O-NFO catalyst are not changed

under OER conditions as displayed in Fig. S16c and d, further proving that the structural transformation is induced by sulfur doping and leaching. The O 1 s XPS spectra of NFO (Fig. 3i) can be divided into 529.3, 530.8 and 532.1 eV corresponding to metal-oxygen (M-O), metal-hydroxide (M-OH) and absorbed water, respectively [31,32]. The positions for M-O and -OH of NFO-S5 are similar to those of NFO. The peak at 530.5 eV for the O-NFO-S5 catalyst is ascribed to metal-oxyhydroxide (M-OOH), suggesting the generation of O_2^{2-} species on the catalyst surface due to the formation of FeOOH resulting from the S leaching and structural transformation [31,32].

3.4. The study of the mechanism for enhanced OER activity by S-doping and leaching

To unlock the mechanism responsible for the S doping and leaching-induced OER performance enhancement, the intrinsic OER activities of NFO, NFO-S5 and O-NFO-S5 were investigated. The relative electrochemically active surface areas (ECSAs) of the samples were measured and calculated according to the charging current in a free of Faradaic process potential window as shown in Fig. S17. As presented in Fig. S17d, the double-layer capacitances (C_{dl}) of NFO, NFO-S5 and O-NFO-S5 are 12.2, 24.3 and 26.2 mF/cm^2, respectively, illustrating a larger active surface area and more active sites for O-NFO-S5 as a result of the S doping and leaching-induced structure transformation. Based on the equation of ECSA $= C_{dl}/C_s \times A$, where C_s is identified as 0.04 mF/cm^2 in 1 M potassium hydroxide according to previous report [33] and A is the effective working area of IF, as shown in Fig. 4a, the ECSA values
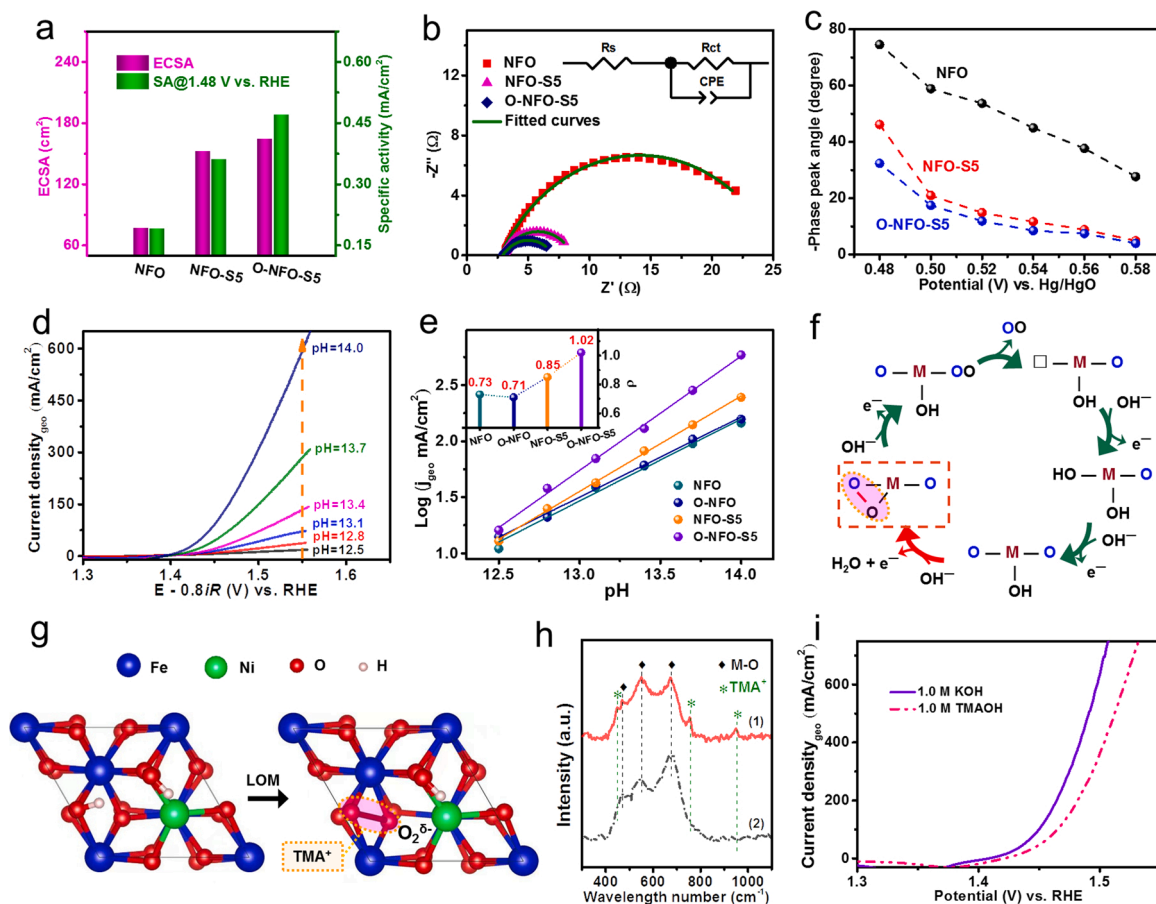
Fig. 4. (a) ECSAs and specific activities (current density j normalized by ECSA) at a potential of 1.48 V vs. RHE for NFO, NFO-S5 and O-NFO-S5. (b) Nyquist plots at an applied potential of 0.52 V vs. Hg/HgO of NFO, NFO-S5 and O-NFO-S5, and the inset is the equivalent circuit model. (c) The phase peak angles of the Bode plots for NFO, NFO-S5 and O-NFO-S5 catalysts at the potential range from 0.48 to 0.58 V vs. Hg/HgO. (d) pH dependence of the OER performances for O-NFO-S5. The potentials were corrected with an 80% *iR* compensation using the following equation: $E_{iR\ corrected} = E - 0.8iR$, where *R* is the solution resistance measured via EIS. (e) Current densities$_{geo}$ (j) of NFO, O-NFO, NFO-S5 and O-NFO-S5 at 1.55 V vs. RHE as a function of the pH value. The inset is the proton reaction orders of the catalysts estimated based on $\rho = (\partial\log(j)/\partial pH)$, where ρ and j are the proton reaction order and current density$_{geo}$ at a constant potential of 1.55 V vs. RHE. (f) Schematic representation for the proposed OER pathway that involves the rate-determining proton transfer decoupled from the electron transfer step. (g) Schematic illustration of the recognition of $O_2^{\delta-}$ species using TMA$^+$ as a chemical probe. (h) Raman spectra of O-NFO-S5 catalysts. These two catalysts were respectively performed at 1.55 V vs. RHE in 1 M TMAOH (red solid line) and 1 M KOH (black dash line) solution, and then were thoroughly washed with deionized water and acetone for the ex situ Raman spectra test. (i) LSV curves of O-NFO-S5 in 1 M TMAOH and 1 M KOH.

of NFO, NFO-S5 and O-NFO-S5 are estimated to be 76.3, 151.8 and 163.7 cm^2, respectively. At a given voltage of 1.48 V vs. RHE, the specific activity of ECSA-normalized current density (current *j* normalized by ECSAs is displayed in Fig. S18) for NFO-S5 (0.36 mA/cm^2) is much larger than that of NFO (0.19 mA/cm^2) due to the S doping, and the specific activity of the O-NFO-S5 catalyst is further increased to 0.47 mA/cm^2 after OER stability test. This demonstrates that the O-NFO-S5 catalyst with a Ni-doped FeOOH phase structure possesses higher intrinsic OER activity than those of undoped or unleached catalysts due to the structure transformation [18,24].

The electrical conductivity and charge transfer kinetics of NFO-S5 before and after S doping and leaching were probed by electrochemical impedance spectroscopy (EIS) measurements as shown in Fig. 4b. It can be found that the O-NFO-S5 catalyst exhibits similar solution resistance (R_s) but a smaller charge-transfer resistance (R_{ct}) of 4.18 Ω than those of the NFO-S5 and NFO catalysts with the R_{ct} values of 5.77 and 22.81 Ω, respectively, suggesting the effect of S doping and leaching on markedly improving the electrical conductivity and promoting the charge transfer of NFO [34]. Besides, Fig. S19 show the Bode plots of NFO, NFO-S5 and O-NFO-S5, respectively, and their peak phase angles are collected in Fig. 4c, which display the smallest phase angles for the O-NFO-S5 catalyst at the same applied voltages, suggesting the

faster OER kinetics of O-NFO-S5 and more electrons are involved in the electrocatalysis than those of NFO and NFO-S5 catalysts [35,36].

According to the conventional adsorbate evolution mechanism (AEM), the OER process is constituted by multiple adsorbed intermediates with highly correlated adsorption strength, and thus the minimum theoretical overpotential is generally larger than 0.37 V [37]. In consideration of the ultralow overpotential (196 mV @ 10 mA/cm^2) obtained for the O-NFO-S5 catalyst in this study, the lattice oxygen oxidation mechanism (LOM) may be reasonable to illustrate its excellent OER activity. The non-concert between the hydroxide affinity and electron transfer kinetics at the catalyst/electrolyte interface results in the pH-dependent OER performance, and the OER process of oxides through the involvement of lattice oxygen shows typical pH-dependent activity on the RHE scale [38–40]. Therefore, the study of the pH dependence on the OER activity could afford further insight into the electrocatalytic mechanism and related intermediates for the as-prepared catalysts. From the pH-dependent OER performance tests as shown in Fig. 4d, O-NFO-S5 exhibits the improved OER activity with the increasing pH from 12.5 to 14. The proton reaction order can be estimated by the following equation $\rho = (\partial\log(j)/\partial pH)$, where ρ is the proton reaction order and j is the current density$_{geo}$ at the potential of 1.55 V vs. RHE [41]. As shown in Figs. S20 and 4d, e, the proton reaction

order for O-NFO-S5 is higher than that of NFO-S5, while there is no significant difference for the proton reaction orders of NFO and O-NFO. This strongest pH dependence feature for O-NFO-S5 indicates that the lattice oxygen redox activity is more sufficiently activated and participates in the OER process due to the S doping and leaching-induced structural transformation, and the chemical deprotonation of *OH is the rate-determining step [37,41]. One possible OER route for O-NFO-S5 is further proposed, which is showed in Fig. 4f, the deprotonation of *OH involves only proton transfer (HO–M(O)–O + OH− → O-(O)M–O + H_2O) and is decoupled from the following electron transfer in the process of the release of oxygen [36,40]. Similar phenomenon has also been reported on other highly covalent oxides and it has been demonstrated that the oxygen redox would generate oxygenated species with negatively charged and hence leads to weak *OH affinity [37,38,41,42]. The recognition of negatively charged oxygenated species ($O_2^{\delta-}$, such as O_2^{2-} and O_2^-) could offer indirect evidence for the above proposed LOM route [37,43]. In order to track these $O_2^{\delta-}$ species from the LOM, tetramethylammonium cation (TMA^+) could be employed as a chemical probe (Fig. 4g) to detect the existence of negative oxygenated intermediates due to their strong electrostatic interaction between TMA^+ and $O_2^{\delta-}$ species [37,44–46]. As shown in the Raman spectra (Fig. 4h), three peaks at 472, 553 and 675 cm^{-1} were ascribed to Metal–Oxygen (M-O) for the O-NFO-S5 catalysts that were treated in 1 M KOH and 1 M tetramethylammonium hydroxide (TMAOH) solution at a constant potential of 1.55 V vs. RHE. Obviously, there are three new emerging peaks centered at 450, 756, and 953 cm^{-1}, which are the characteristic peaks of TMA^+ [37,41], can be observed when the O-NFO-S5 catalyst was operated at a fixed potential of 1.55 V vs. RHE in TMAOH electrolyte. This demonstrates that TMA^+ strongly binds to the catalyst surface via interacting with the produced negative oxygenated species during the OER process. Furthermore, Fig. 4i presents the OER activities of O-NFO-S5 in 1 M KOH and TMAOH solution, a significant reduced OER activity and increased Tafel slope from 22.8 to 41.2 mV/dec (Fig. S21) can be observed in 1 M TMAOH solution owing to the inhibition of the LOM resulting from the strong binding of TMA^+ and negative oxygenated intermediates.

On the basis of the above component, structural and mechanism characterizations and analysis, the fascinating OER activity of the O-NFO-S5 electrocatalyst could be thus ascribed to the following aspects:

(i) the structure of the catalyst converts from LDHs to highly active oxyhydroxides because of the leaching of S [18,24]; (ii) the electronic structure Fe species which may possesses high OER activity [47,48] is optimized and the lattice oxygen is sufficiently activated and participates in the OER process due to the S doping and leaching-induced structural transformation; (iii) the strong synergistic effect between Fe and Ni promotes the reaction kinetics and provides a favorable electronic structure for the OER [49–51]; (iv) the self-supported nanosheet-like structure is beneficial to exposure more active sits and accelerate the electron transfer from the surface electrocatalyst to the conductive core; (v) the catalyst *in-suit* grows on a self-supported conductive substrate, and thus the polymer binders do not need to be used in the preparation of electrocatalysts, which could avoid the possibility of masking the exposure of active sites, decrease interface contact resistance, and conduce mechanical and electrocatalytic stability, ultimately resulting in an improved electrocatalytic performance.

3.5. Electrochemical HER activities of NFO-Sx

To verify the possible application of our electrocatalyst in practical water splitting system, the HER activities of the as-prepared NFO-Sx catalysts were also explored and their LSV curves are presented in Fig. 5a. The overpotentials of NFO-Sx catalysts at the current density$_{geo}$ of 100 mA/cm^2 are summarized in Fig. 5b, and it can be observed that the NFO-S60 catalyst shows an excellent HER activity and requires a low overpotential of 195 mV to obtain 100 mA/cm^2, which is lower than those of other NFO-Sx samples mainly due to the formation of a large number of metal sulfides with high HER activity 52. The corresponding Tafel slope (Fig. 5c) of NFO-S60 shows the lowest value (109 mV/dec) among the NFO-Sx catalysts, suggesting its fast HER kinetics. The Tafel curves of the samples for the HER are derived from steady state chronoamperometric measurements [25] as shown in Figs. S22–S28. The long-term stability of the best-performing HER catalyst NFO-S60 was also measured for six continuous stages at current densities$_{geo}$ of 10, 20, 50, 100, 300, and 10 mA/cm^2 for a total time of 150 h as shown in Fig. 5d. Surprisingly, a current density$_{geo}$ 10 mA/cm^2 in the last stage requires ∼ 58 mV less than that of the first stage just like the OER performance, which can also be testified by the HER LSV curves of NFO-S60 before and after HER durability test as displayed in Fig. 5e.
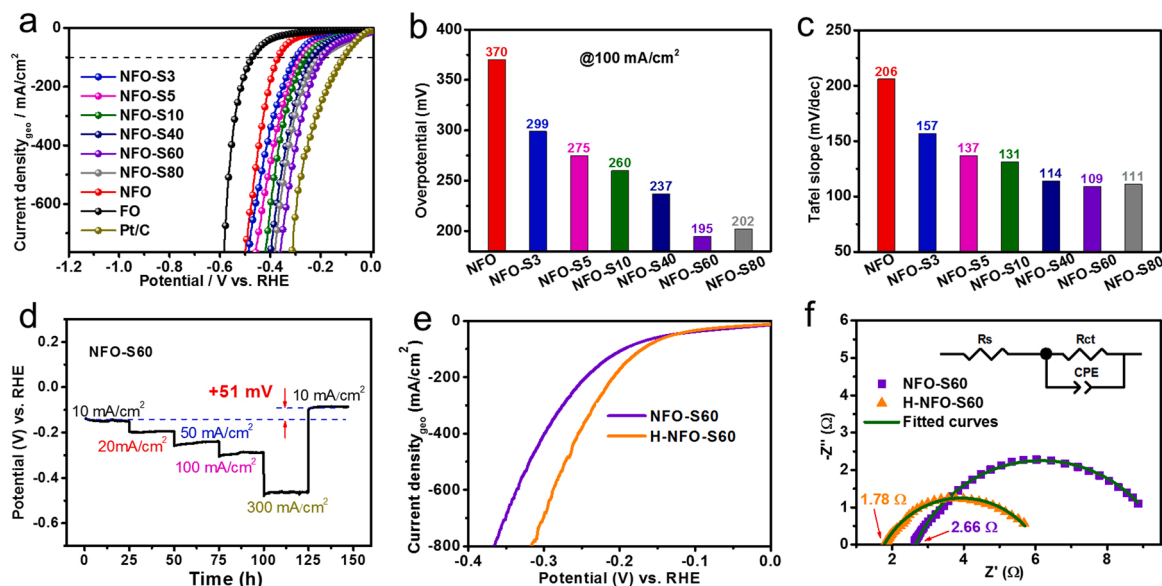

Fig. 5. (a) LSV curves for the HER, (b) overpotential comparison at the current density$_{geo}$ of 100 mA/cm^2 and (c) Summarized Tafel slopes of NFO-Sx derived from steady state chronoamperometric measurements. (d) Chronopotentiometry of NFO-S60 at the current densities$_{geo}$ of 10, 20, 50, 100, 300 and 10 mA/cm^2 for a total time of 150 h. (e) LSV curves of NFO-S60 before and after HER stability test. (f) Nyquist plots at an applied potential of −1.10 V vs. Hg/HgO of NFO-S60 and H-NFO-S60, and the inset is the equivalent circuit model.

This phenomenon can be further confirmed by the chronoamperometric stability measurement as shown in Fig. S29, which demonstrates that after four continuous stages at the potentials of −0.1, −0.2, −0.3, and −0.4 V vs. RHE, in the last stage, the obtained current density$_{geo}$ is ~ 6.3 mA/cm^2 higher than the first stage. The overpotential of NFO-S60 after HER stability test (denoted as H-NFO-S60) at the current density$_{geo}$ 100 mA/cm^2 is 168 mV and its Tafel slope is 102 mV/dec (Fig. S30), both of which are lower than those of NFO-S60 before HER stability test (an overpotential of 195 mV at 100 mA/cm^2 and a Tafel slope of 109 mV/dec). Additionally, the best-performing HER catalyst H-NFO-S60 shows strong long-term stability over 100 h as displayed in the chronoamperometric durability test (Fig. S31).

To probe the reason for the enhanced HER activity, the XRD pattern of H-NFO-S60 (Fig. S32) was carried out firstly, which shows that the phase of H-NFO-S60 still remained as before. The intrinsic HER activities of NFO-S60 and H-NFO-S60 were estimated by the specific activity normalized by ECSAs as shown in Fig. S33. The calculated ECSAs for the NFO-S60 and H-NFO-S60 are 870.0 and 1282.5 cm^2, respectively, while there is no obvious difference between their specific activities of ECSA-normalized current density, suggesting the intrinsic HER activity of NFO-S60 has not been changed under HER condition, which is associated with the unchanged phase structure of NFO-S60 after HER stability test. As shown in Fig. S34, the magnified SEM images indicate that there

is no distinct change between before and after HER stability measurement, while the SEM images with low magnification exhibit the aggregates on the surface of IF have been removed after HER test, which may facilitate the mass and charge transfer at the interface between electrode and solution. In addition, as presented in Fig. 5f, the fitted results of Nyquist plots illustrate the R_s of H-NFO-S60 is 1.78 Ω, which is much lower than NFO-S60 with a R_s of 2.66 Ω, demonstrating the charge transfer at the interface between electrode and solution has been improved due to the loss of the aggregates [34]. The smaller R_{ct} value of H-NFO-S60 (4.30 Ω) compared with that of NFO-S60 (6.98 Ω) indicates that the charge transfer of the H-NFO-S60 catalyst was also boosted after HER stability test.

3.6. Electrochemical overall water splitting evaluation

Inspired by the electrocatalytic activities of NFO-Sx samples with tunable bifunctionality for the OER and HER, we fabricated a two-electrode system (Fig. 6a) to explore the overall water splitting performance by using the NFO-S5 and NFO-S60 as the anode and cathode, respectively, [i.e., NFO-S5(+)||NFO-S60(−)]. The RuO$_2$(+)||Pt/C(−), NFO-S5(+)||NFO-S5(−), NFO-S60(+)||NFO-S60(−) and NFO-S60(+)||NFO-S5(−) devices were also investigated for comparison. As displayed in Fig. 6b, NFO-S5(+)||NFO-S60(−) exhibits the best overall water
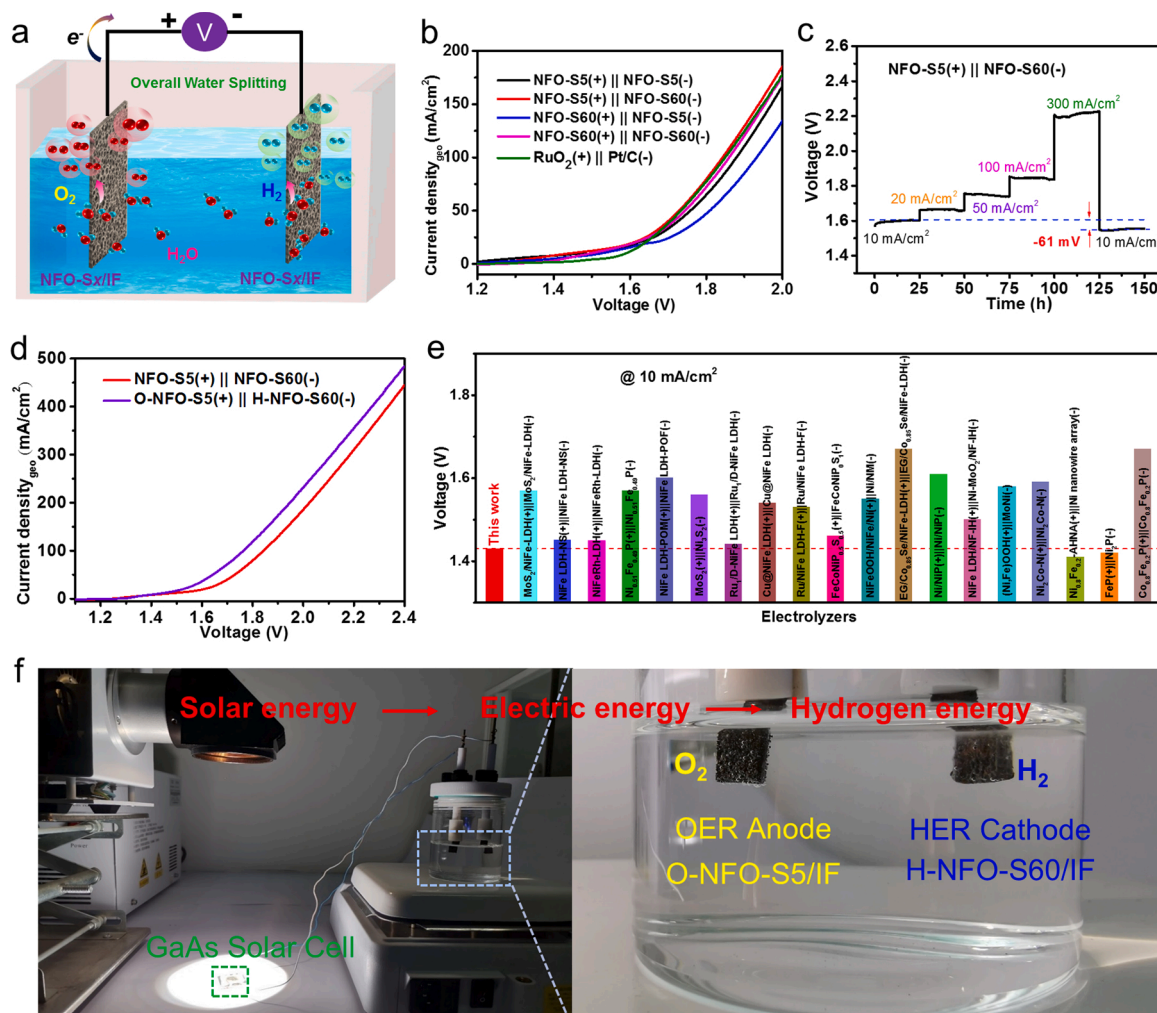

Fig. 6. (a) Schematic illustration of the two-electrode cell for overall water splitting. (b) LSV curves for water overall splitting of NFO-S5(+)||NFO-S60(−), NFO-S5(+)||NFO-S5(−), NFO-S60(+)||NFO-S60(−), NFO-S60(+)||NFO-S5(−) and RuO$_2$(+)||Pt/C(−) systems. (c) Chronopotentiometry of NFO-S5(+)||NFO-S60(−) device at the current densities$_{geo}$ of 10, 20, 50, 100, 300 and 10 mA/cm^2 for a total time of 150 h. (d) LSV curves of NFO-S5(+)||NFO-S60(−) device before and after stability test. (e) Voltage comparison at the current density$_{geo}$ of 10 mA/cm^2 with recent reported water overall splitting systems. (f) Digital photograph of the overall water splitting device driven by a commercial GaAs solar cell to obtain the energy conversion from solar energy to hydrogen energy.

splitting activity among above systems due to the outstanding OER and HER performances for NFO-S5 and NFO-S60, respectively, suggesting that the catalysts with tunable bifunctionality could be prepared by rationally regulating the content of S to meet practical applications. The long-term stability of the best-performing system NFO-S5(+)||NFO-S60 (−) was tested for six successive stages at current densities$_{geo}$ of 10, 20, 50, 100, 300, and 10 mA/cm^2 for a total time of 150 h as shown in Fig. 6c. Impressively, a current density$_{geo}$ 10 mA/cm^2 in the last stage. requires 61 mV less than that of the first stage just like the OER and HER performances, which also been testified by the LSV curves of NFO-S5(+)||NFO-S60(−) before and after full water electrolysis durability test as displayed in Fig. 6d. The two-electrode system after water electrolysis durability test was denoted as O-NFO-S5(+)||H-NFO-S60(−), which requires an ultralow voltage of 1.43 V to achieve a current density$_{geo}$ of 10 mA/cm^2, which superior to most recent reported water splitting devices as shown in Fig. 6e and Table S2. The Faradaic efficiencies for O$_2$ and H$_2$ production of O-NFO-S5(+)||H-NFO-S60(−) were also estimated by employing the water drainage method [53] as presented in Fig. S35a. It can be observed that the volume ratio for produced O$_2$ and H$_2$ is equal to 1:2, and the measured amount of O$_2$ and H$_2$ gases matches well with their corresponding calculated results (Fig. S35b), indicating ~ 100% Faradaic efficiencies for both the OER and HER processes in the overall water splitting. A desired environmental-friendly and sustainable path to produce hydrogen energy is electrocatalytic water splitting driven by the electrical energy generated via solar cells, and therefore an energy conversion system was assembled as shown in Fig. 6f, which could convert the solar energy to hydrogen energy by using a commercial GaAs solar cell (its specifications can be found in Table S3) to drive water splitting and O-NFO-S5 (+)||H-NFO-S60(−) as the water electrolysis electrodes. The solar-to-hydrogen device continually produces abundant O$_2$ and H$_2$ bubbles as displayed in Video S1, which demonstrates that it is feasible to develop nonprecious-metal-based water-splitting electrocatalysts for practical applications by utilizing a solar energy→electric energy→hydrogen energy conversion device without an additional applied bias.

Supplementary material related to this article can be found online at doi:10.1016/j.apcatb.2021.121030.

4. Conclusions

In summary, a series of OER and HER catalysts were manufactured by a one-pot hydrothermal method solely based on earth-abundant elements. We found that tunable regulation on the compositions as well as the structural properties of the as-obtained electrocatalysts and thus electrocatalytic activity can be accomplished by rationally modulating the non-metal element of S in the catalyst via doping and leaching for the first time. The NiFe-based catalyst with S doping is demonstrated to achieve complete electrochemical structure reconstruction (ESR) accompanied by the leaching of S into highly active Ni-doped Fe-oxy-hydroxides (Ni-FeOOH) exhibiting sufficient activation of lattice oxygen redox reactions, while the NiFe-based catalyst without S doping does not appear ESR. Under optimal conditions, the O-NFO-S5 electrocatalyst with structure reconstruction induced by S-doping/leaching exhibits low overpotentials of 196 and 224 mV to obtain current densities$_{geo}$ of 10 and 100 mA/cm^2 for the OER and a small Tafel slope of 22.8 mV/dec, respectively. The H-NFO-S60 electrocatalyst displays an overpotential of only 167 mV at the current density$_{geo}$ of 100 mA/cm^2 and a small Tafel slope of 102 mV/dec towards the HER. When the OER and HER electrocatalysts with best performances are constructed into a two-electrode overall water splitting device, a current density$_{geo}$ of 10 mA/cm^2 can be achieved at an ultralow cell voltage of 1.43 V, which is much superior to most ever reported two-electrode overall water splitting systems at the same current density$_{geo}$. Our work not only affords a series of high-performance and stable catalysts and their facile and inexpensive synthetic route for electrochemical water electrolysis but also highlights the significance of dual compositions and structure regulation through an in situ non-metal element doping and leaching-induced strategy towards the optimization of individual OER and HER.

CRediT authorship contribution statement

Xiang Chen: Conceptualization, Investigation, Methodology, Visualization, Writing – original draft, Funding acquisition. **Zhaojian Qiu:** Investigation, Validation, Visualization. **Hanlu Xing:** Investigation, Validation. **Shunxin Fei:** Methodology, Investigation. **Junzhe Li:** Methodology, Formal analysis. **Lianbo Ma:** Visualization, Writing – review & editing. **Yongtao Li:** Methodology, Formal analysis. **Dongming Liu:** Writing – review & editing, Supervision, Funding acquisition.

Declaration of Competing Interest

The authors declare that they have no known competing financial interests or personal relationships that could have appeared to influence the work reported in this paper.

Appendix A. Supplementary material

Supporting Information Available: SEM images and TEM images, XRD patterns, LSV curves normalized by ECSAs, digital photograph and tables of comparison of the electrocatalytic activity with others and video of the solar energy-electric energy-hydrogen energy conversion system.

Supplementary data associated with this article can be found in the online version at doi:10.1016/j.apcatb.2021.121030.

References

[1] I. Roger, M.A. Shipman, M.D. Symes, Earth-abundant catalysts for electrochemical and photoelectrochemical water splitting, Nat. Rev. Chem. 1 (2017) 1–13.

[2] K. Wu, K. Sun, S. Liu, W.C. Cheong, Z. Chen, C. Zhang, Y. Pan, Y. Cheng, Z. Zhuang, X. Wei, Y. Wang, L. Zheng, Q. Zhang, D. Wang, Q. Peng, C. Chen, Y. Li, Atomically dispersed Ni-Ru-P interface sites for high-efficiency pH-universal electrocatalysis of hydrogen evolution, Nano Energy 80 (2021), 105467.

[3] J. Song, C. Wei, Z.F. Huang, C. Liu, L. Zeng, X. Wang, Z.J. Xu, A review on fundamentals for designing oxygen evolution electrocatalysts, Chem. Soc. Rev. 49 (2020) 2196–2214.

[4] T. Sun, L. Xu, D. Wang, Y. Li, Metal organic frameworks derived single atom catalysts for electrocatalytic energy conversion, Nano Res. 12 (2019) 2067–2080.

[5] C. Hu, L. Zhang, J. Gong, Recent progress made in the mechanism comprehension and design of electrocatalysts for alkaline water splitting, Energy Environ. Sci. 12 (2019) 2620–2645.

[6] C. Wang, L. Jin, H. Shang, H. Xu, Y. Shiraishi, Y. Du, Advances in engineering RuO$_2$ electrocatalysts towards oxygen evolution reaction, Chin. Chem. Lett. 32 (2021) 2108–2116.

[7] A. Zagalskaya, V. Alexandrov, Role of defects in the interplay between adsorbate evolving and lattice oxygen mechanisms of the oxygen evolution reaction in RuO$_2$ and IrO$_2$, ACS Catal. 10 (2020) 3650–3657.

[8] a) P. Zhou, X. Lv, D. Xing, F. Ma, Y. Liu, Z. Wang, P. Wang, Z. Zheng, Y. Dai, B. Huang, High-efficient electrocatalytic overall water splitting over vanadium doped hexagonal Ni$_{0.2}$Mo$_{0.8}$N, Appl. Catal. B Environ. 263 (2020), 118330;
b) X. Chen, H.N. Wang, B. Xia, R.R. Meng, Noncovalent phosphorylation of CoCr layered double hydroxide nanosheets with improved electrocatalytic activity for the oxygen evolution reaction, Chem. Commun. 55 (2019) 12076–12079;
c) B. Jiang, W. Cheong, R. Tu, K. Sun, S. Liu, K. Wu, H. Shang, A. Huang, M. Wang, L. Zheng, X. Wei, C. Chen, Regulating the electronic structure of NiFe layered double hydroxide/reduced graphene oxide by Mn incorporation for high-efficiency oxygen evolution reaction, Sci. China Mater. 64 (2021) 2729–2738.

[9] a) C. Wu, H. Li, Z. Xia, X. Zhang, R. Deng, S. Wang, G. Sun, NiFe layered double hydroxides with unsaturated metal sites via precovered surface strategy for oxygen evolution reaction, ACS Catal. 10 (2020) 11127–11135;
b) J. Choi, D. Kim, W. Zheng, B. Yan, Y. Li, L.Y.S. Lee, Y. Piao, Interface

engineered NiFe$_2$O$_{4-x}$/NiMoO$_4$ nanowire arrays for electrochemical oxygen evolution, Appl. Catal. B Environ. 286 (2021), 119857.

[10] a) J. Yu, F. Yu, M.F. Yuen, C. Wang, Two-dimensional layered double hydroxides as a platform for electrocatalytic oxygen evolution, J. Mater. Chem. A 9 (2021) 9389–9430;
b) X. Chen, Z.J. Qiu, H.L. Xing, S.X. Fei, L.B. Ma, Tertiary-amine-assisted synthesis of hierarchical porous nitrogen-incorporated cobalt–iron (oxy)hydroxide nanosheets for improved oxygen evolution reaction, ACS Appl. Energy Mater. 9 (2021) 8866–8874.

[11] a) D. Zhou, S. Wang, Y. Jia, X. Xiong, H. Yang, S. Liu, J. Tang, J. Zhang, D. Liu, L. Zheng, Y. Kuang, X. Sun, B. Liu, NiFe hydroxide lattice tensile strain: enhancement of adsorption of oxygenated intermediates for efficient water oxidation catalysis, Angew. Chem. Int. Ed. 58 (2019) 736–740;
b) Z. Yuan, S.M. Bak, P. Li, Y. Jia, L. Zheng, Y. Zhou, L. Bai, E. Hu, X.Q. Yang, Z. Cai, Y. Sun, X. Sun, Activating layered double hydroxide with multivacancies by memory effect for energy-efficient hydrogen production at neutral pH, ACS Energy Lett. 4 (2019) 1412–1418;
c) H. Chen, Y. Zou, J. Li, K. Zhang, Y. Xia, B. Hui, D. Yang, Wood aerogel-derived sandwich-like layered nanoelectrodes for alkaline overall seawater electrosplitting, Appl. Catal. B Environ. 293 (2021), 120215.

[12] a) M.B. Stevens, L.J. Enman, E.H. Korkus, J. Zaffran, C.D.M. Trang, J. Asbury, M. G. Kast, M.C. Toroker, S.W. Boettcher, Ternary Ni-Co-Fe oxyhydroxide oxygen evolution catalysts: Intrinsic activity trends, electrical conductivity, and electronic band structure, Nano Res. 12 (2019) 2288–2295;
b) F. Zhang, Y. Shi, T. Xue, J. Zhang, Y. Liang, B. Zhang, In situ electrochemically converting Fe$_2$O$_3$-Ni(OH)$_2$ to NiFe$_2$O$_4$-NiOOH: a highly efficient electrocatalyst towards water oxidation, Sci. China Mater. 60 (2017) 324–334.

[13] a) G. Chen, H. Wan, W. Ma, N. Zhang, Y. Cao, X. Liu, J. Wang, R. Ma, Layered metal hydroxides and their derivatives: controllable synthesis, chemical exfoliation, and electrocatalytic applications, Adv. Energy Mater. 10 (2020) 1902535;
b) D. Li, W. Zhang, J. Zeng, B. Gao, Y. Tang, Q. Gao, Nickel-doped Co$_4$N nanowire bundles as efficient electrocatalysts for oxygen evolution reaction, Sci. China Mater. 64 (2021) 1889–1899;
c) T. Liu, P. Diao, Nickel foam supported Cr-doped NiCo$_2$O$_4$/FeOOH nanoneedle arrays as a high-performance bifunctional electrocatalyst for overall water splitting, Nano Res. 13 (2020) 3299–3309.

[14] a) L. Huang, Z. He, J. Guo, S. Pei, H. Shao, J. Wang, Photodeposition fabrication of hierarchical layered Co-doped Ni oxyhydroxide (Ni$_x$Co$_{1-x}$OOH) catalysts with enhanced electrocatalytic performance for oxygen evolution reaction, Nano Res. 13 (2020) 246–254;
b) W. Hao, D. Yao, Q. Xu, R. Wang, C. Zhang, Y. Guo, R. Sun, M. Huang, Z. Chen, Highly efficient overall-water splitting enabled via grafting boron-inserted Fe-Ni solid solution nanosheets onto unconventional skeleton, Appl. Catal. B Environ. 292 (2021), 120188;
c) X. Chen, H.N. Wang, R.R. Meng, B. Xia, Z.J. Ma, Cadmium hydroxide: a missing non-noble metal hydroxide electrocatalyst for the oxygen evolution reaction, ACS Appl. Energy Mater. 3 (2020) 1305–1310.

[15] B. Zhang, L. Wang, Z. Cao, S.M. Kozlov, F.P. Garcia de Arquer, C.T. Dinh, J. Li, Z. Wang, X. Zheng, L. Zhang, Y. Wen, O. Voznyy, R. Comin, P. De Luna, T. Regier, W. Bi, E.E. Alp, C.W. Pao, L. Zheng, Y. Hu, Y. Ji, Y. Li, Y. Zhang, L. Cavallo, H. Peng, E.H. Sargent, High-valence metals improve oxygen evolution reaction performance by modulating 3d metal oxidation cycle energetics, Nat. Catal. 3 (2020) 985–992.

[16] a) X. Liu, K. Ni, B. Wen, R. Guo, C. Niu, J. Meng, Q. Li, P. Wu, Y. Zhu, X. Wu, L. Mai, Deep reconstruction of nickel-based precatalysts for water oxidation catalysis, ACS Energy Lett. 4 (2019) 2585–2592;
b) T. Wu, S. Sun, J. Song, S. Xi, Y. Du, B. Chen, W.A. Sasangka, H. Liao, C.L. Gan, G.G. Scherer, L. Zeng, H. Wang, H. Li, A. Grimaud, Z.J. Xu, Iron-facilitated dynamic active-site generation on spinel CoAl$_2$O$_4$ with self-termination of surface reconstruction for water oxidation, Nat. Catal. 2 (2019) 763–772;
c) A. Sivanantham, P. Ganesan, A. Vinu, S. Shanmugam, Surface activation and reconstruction of non-oxide-based catalysts through in situ electrochemical tuning for oxygen evolution reactions in alkaline media, ACS Catal. 10 (2020) 463–493;
d) Y. Li, X. Du, J. Huang, C. Wu, Y. Sun, G. Zou, C. Yang, J. Xiong, Recent progress on surface reconstruction of earth-abundant electrocatalysts for water oxidation, Small 15 (2019) 1901980;
e) Z. Zheng, R. Zheng, M. Graś, W. Wei, G. Lota, H. Chen, B.J. Ni, Tuning electronic property and surface reconstruction of amorphous iron borides via W-P co-doping for highly efficient oxygen evolution, Appl. Catal. B Environ. 288 (2021), 120037.

[17] B. Zhang, K. Jiang, H. Wang, S. Hu, Fluoride-induced dynamic surface self-reconstruction produces unexpectedly efficient oxygen-evolution catalyst, Nano Lett. 19 (2019) 530–537.

[18] N.C.S. Selvam, L. Du, B.Y. Xia, P.J. Yoo, B. You, Reconstructed water oxidation electrocatalysts: the impact of surface dynamics on intrinsic activities, Adv. Funct. Mater. 31 (2021), 2008190.

[19] L. Liu, A. Corma, Structural transformations of solid electrocatalysts and photocatalysts, Nat. Rev. Chem. 5 (2021) 256–276.

[20] C.X. Zhao, B.Q. Li, M. Zhao, J.N. Liu, L.D. Zhao, X. Chen, Q. Zhang, Precise anionic regulation of NiFe hydroxysulfide assisted by electrochemical reactions for efficient electrocatalysis, Energy Environ. Sci. 13 (2020) 1711–1716.

[21] Y. Duan, J.Y. Lee, S. Xi, Y. Sun, J. Ge, S.J. Hong, Y. Chen, S. Dou, F. Meng, C. Diao, A.C. Fisher, X. Wang, G.G. Scherer, A. Grimaud, Z.J. Xu, Anodic oxidation enabled cation leaching for promoting surface reconstruction in water oxidation, Angew. Chem. Int. Ed. 60 (2021) 7418–7425.

[22] H.F. Wang, C. Tang, B.Q. Li, Q. Zhang, A review of anion-regulated multi-anion transition metal compounds for oxygen evolution electrocatalysis, Inorg. Chem. Front. 5 (2018) 521–534.

[23] S. Li, Z. Li, R. Ma, C. Gao, L. Liu, L. Hu, J. Zhu, T. Sun, Y. Tang, D. Liu, J. Wang, A glass-ceramic with accelerated surface reconstruction toward the efficient oxygen evolution reaction, Angew. Chem. Int. Ed. 60 (2021) 3773–3780.

[24] J. Liu, P. Ding, Z. Zhu, W. Du, X. Xu, J. Hu, Y. Zhou, H. Zeng, Engineering self-reconstruction via flexible components in layered double hydroxides for superior-evolving performance, Small (2021), 2101671.

[25] S. Anantharaj, S. Noda, M. Driess, P.W. Menezes, The pitfalls of using potentiodynamic polarization curves for tafel analysis in electrocatalytic water splitting, ACS Energy Lett. 6 (2021) 1607–1611.

[26] Y. Yang, Y. Kang, H. Zhao, X. Dai, M. Cui, X. Luan, X. Zhang, F. Nie, Z. Ren, W. Song, An interfacial electron transfer on tetrahedral NiS$_2$/NiSe$_2$ heterocages with dual-phase synergy for efficiently triggering the oxygen evolution reaction, Small 16 (2020), 1905083.

[27] X. Wang, W. Ma, C. Ding, Z. Xu, H. Wang, X. Zong, C. Li, Amorphous multi-elements electrocatalysts with tunable bifunctionality toward overall water splitting, ACS Catal. 8 (2018) 9926–9935.

[28] B. Wu, L. Su, X. Dai, X. Chai, Development of sludge-derived mesoporous material with loaded nano CaO$_2$ and doped Fe for re-utilization of dewatered waste-activated sludge as dewatering aids, Chem. Eng. J. 335 (2018) 161–168.

[29] T. Yamashita, P. Hayes, Analysis of XPS spectra of Fe$_{2+}$ and Fe^{3+} ions in oxide materials, Appl. Surf. Sci. 254 (2008) 2441–2449.

[30] A.P. Grosvenor, B.A. Kobe, M.C. Biesinger, N.S. McIntyre, Investigation of multiplet splitting of iron 2p XPS spectra and bonding in iron compounds, Surf. Interface Anal. 36 (2004) 1564–1574.

[31] X. Gao, Y. Yu, Q. Liang, Y. Pang, L. Miao, X. Liu, Z. Kou, J. He, S.J. Pennycook, S. Mu, J. Wang, Surface nitridation of nickel-cobalt alloy nanocactoids raises the performance of water oxidation and splitting, Appl. Catal. B Environ. 270 (2020), 118889.

[32] J. Masa, I. Sinev, H. Mistry, E. Ventosa, M. de la Mata, J. Arbiol, M. Muhler, B. R. Cuenya, W. Schuhmann, Ultrathin high surface area nickel boride (NixB) nanosheets as highly efficient electrocatalyst for oxygen evolution, Adv. Energy Mater. 7 (2017), 1700381.

[33] S. Niu, W.J. Jiang, Z. Wei, T. Tang, J. Ma, J.S. Hu, L.J. Wan, Se-doping activates FeOOH for cost-effective and efficient electrochemical water oxidation, J. Am. Chem. Soc. 141 (2019) 7005–7013.

[34] G. Rajeshkhanna, S. Kandula, K.R. Shrestha, N.H. Kim, J.H. Lee, A. New, Class of Zn$_{1-x}$Fe$_x$-oxyselenide and Zn$_{1-x}$Fe$_x$-LDH nanostructured material with remarkable bifunctional oxygen and hydrogen evolution electrocatalytic activities for overall water splitting, Small 14 (2018), 1803638.

[35] D. Zhou, S. Wang, Y. Jia, X. Xiong, H. Yang, S. Liu, J. Tang, J. Zhang, D. Liu, L. Zheng, Y. Kuang, X. Sun, B. Liu, NiFe hydroxide lattice tensile strain: enhancement of adsorption of oxygenated intermediates for efficient water oxidation catalysis, Angew. Chem. Int. Ed. 58 (2019) 736–740.

[36] J. He, Y. Liu, Y. Huang, H. Li, Y. Zou, C.L. Dong, S. Wang, Fe^{2+}-induced in situ intercalation and cation exsolution of Co$_{80}$Fe$_{20}$(OH)(OCH$_3$) with rich vacancies for boosting oxygen evolution reaction, Adv. Funct. Mater. 31 (2021), 2009245.

[37] Z.F. Huang, J. Song, Y. Du, S. Xi, S. Dou, J.M.V. Nsanzimana, C. Wang, Z.J. Xu, X. Wang, Chemical and structural origin of lattice oxygen oxidation in Co-Zn oxyhydroxide oxygen evolution electrocatalysts, Nat. Energy 4 (2019) 329–338.

[38] A. Grimaud, O. Diaz-Morales, B. Han, W.T. Hong, Y.L. Lee, L. Giordano, K. A. Stoerzinger, M.T.M. Koper, Y.S. Horn, Activating lattice oxygen redox reactions in metal oxides to catalyse oxygen evolution, Nat. Chem. 9 (2017) 457–465.

[39] N. Zhang, Y. Chai, Lattice oxygen redox chemistry in solid-state electrocatalysts for water oxidation, Energy Environ. Sci. 14 (2021) 4647–4671.

[40] T. Liu, M. Guo, A. Orthaber, R. Lomoth, M. Lundberg, S. Ott, L. Hammarström, Accelerating proton-coupled electron transfer of metal hydrides in catalyst model reactions, Nat. Chem. 10 (2018) 881–887.

[41] Z.F. Huang, S. Xi, J. Song, S. Dou, X. Li, Y. Du, C. Diao, Z.J. Xu, X. Wang, Tuning of lattice oxygen reactivity and scaling relation to construct better oxygen evolution electrocatalyst, Nat. Commun. 12 (2021) 3992.

[42] W.T. Hong, K.A. Stoerzinger, Y.L. Lee, L. Giordano, A. Grimaud, A.M. Johnson, J. Hwang, E.J. Crumlin, W. Yang, Y. Shao-Horn, Charge-transfer-energy-dependent oxygen evolution reaction mechanisms for perovskite oxides, Energy Environ. Sci. 10 (2017) 2190–2200.

[43] G. Assat, J.M. Tarascon, Fundamental understanding and practical challenges of anionic redox activity in Li-ion batteries, Nat. Energy 3 (2018) 373–386.

[44] Y. Lei, T. Xu, S. Ye, L. Zheng, P. Liao, W. Xiong, J. Hu, Y. Wang, J. Wang, X. Ren, C. He, Q. Zhang, J. Liu, X. Sun, Engineering defect-rich Fe-doped NiO coupled Ni cluster nanotube arrays with excellent oxygen evolution activity, Appl. Catal. B Environ. 285 (2021), 119809.

[45] C. Yang, O. Fontaine, J.M. Tarascon, A. Grimaud, Chemical recognition of active oxygen species on the surface of oxygen evolution reaction electrocatalysts, Angew. Chem. Int. Ed. 56 (2017) 8652–8656.

[46] B.J. Trzesniewski, O.D. Morales, D.A. Vermaas, A. Longo, W. Bras, M.T.M. Koper, W.A. Smith, In situ observation of active oxygen species in Fe-containing Ni-based oxygen evolution catalysts: the effect of pH on electrochemical activity, J. Am. Chem. Soc. 137 (2015) 15112–15121.

[47] H.S. Ahn, A.J. Bard, Surface interrogation scanning electrochemical microscopy of Ni$_{1-x}$Fe$_x$OOH (0 < x < 0.27) oxygen evolving catalyst: kinetics of the "fast" iron sites, J. Am. Chem. Soc. 138 (2016) 313–318.

[48] X. Han, C. Yu, S. Zhou, C. Zhao, H. Huang, J. Yang, Z. Liu, J. Zhao, J. Qiu, Ultrasensitive iron-triggered nanosized Fe-CoOOH integrated with graphene for highly efficient oxygen evolution, Adv. Energy Mater. 7 (2017), 1602148.

[49] C.F. Li, J.W. Zhao, L.J. Xie, J.Q. Wu, G.R. Li, Fe doping and oxygen vacancy modulated Fe-Ni$_5$P$_4$/NiFeOH nanosheets as bifunctional electrocatalysts for efficient overall water splitting, Appl. Catal. B Environ. 291 (2021), 119987.

[50] L. Trotochaud, S.L. Young, J.K. Ranney, S.W. Boettcher, Nickel–iron oxyhydroxide oxygen-evolution electrocatalysts: the role of intentional and incidental iron incorporation, J. Am. Chem. Soc. 136 (2014) 6744–6753.

[51] Y.N. Zhou, W.L. Yu, Y.N. Cao, J. Zhao, B. Dong, Y. Ma, F.L. Wang, R.Y. Fan, Y. L. Zhou, Y.M. Chai, S-doped nickel-iron hydroxides synthesized by room-temperature electrochemical activation for efficient oxygen evolution, Appl. Catal. B Environ. 292 (2021), 120150.

[52] a) P. Chen, T. Zhou, M. Zhang, Y. Tong, C. Zhong, N. Zhang, L. Zhang, C. Wu, Y. Xie, 3D nitrogen-anion-decorated nickel sulfides for highly efficient overall water splitting, Adv. Mater. 29 (2017) 1701584;
b) M. Wang, L. Zhang, J. Pan, M. Huang, H. Zhu, A highly efficient Fe-doped Ni$_3$S$_2$ electrocatalyst for overall water splitting, Nano Res. (2021), https://doi.org/10.1007/s12274-021-3416-5;
c) C. Yang, M.Y. Gao, Q.B. Zhang, J.R. Zeng, X.T. Li, A.P. Abbott, In-situ activation of self-supported 3D hierarchically porous Ni$_3$S$_2$ films grown on nanoporous copper as excellent pH-universal electrocatalysts for hydrogen evolution reaction, Nano Energy 36 (2017) 85–1701594;
d) H. Su, S. Song, S. Li, Y. Gao, L. Ge, W. Song, T. Ma, J. Liu, High-valent bimetal Ni$_3$S$_2$/Co$_3$S$_4$ induced by Cu doping for bifunctional electrocatalytic water splitting, Appl. Catal. B Environ. 293 (2021), 120225.

[53] C. Liang, P. Zou, A. Nairan, Y. Zhang, J. Liu, K. Liu, S. Hu, F. Kang, H. Fan, C. Yang, Exceptional performance of hierarchical Ni-Fe oxyhydroxide@NiFe alloy nanowire array electrocatalysts for large current density water splitting, Energy Environ. Sci. 13 (2020) 86–95.